HAL
open science

Rupture properties of the 2020 Mw 6.8 Calama (northern Chile) intraslab earthquake. Comparison with similar intraslab events in the region

Carlos Herrera, Francisco Pastén-Araya, Leoncio Cabrera, Bertrand Potin, Efraín Rivera, Sergio Ruiz, Raúl Madariaga, Eduardo Contreras-Reyes

To cite this version:

Carlos Herrera, Francisco Pastén-Araya, Leoncio Cabrera, Bertrand Potin, Efraín Rivera, et al.. Rupture properties of the 2020 Mw 6.8 Calama (northern Chile) intraslab earthquake. Comparison with similar intraslab events in the region. Geophysical Journal International, 2022, 10.1093/gji/ggac434 . insu-03861042

HAL Id: insu-03861042

https://insu.hal.science/insu-03861042

Submitted on 11 May 2023

HAL is a multi-disciplinary open access archive for the deposit and dissemination of scientific research documents, whether they are published or not. The documents may come from teaching and research institutions in France or abroad, or from public or private research centers.

L'archive ouverte pluridisciplinaire **HAL**, est destinée au dépôt et à la diffusion de documents scientifiques de niveau recherche, publiés ou non, émanant des établissements d'enseignement et de recherche français ou étrangers, des laboratoires publics ou privés.

Geophysical Journal International

Geophys. J. Int. (2023) **232,** 2070–2079
Advance Access publication 2022 November 03
GJI Seismology

https://doi.org/10.1093/gji/ggac434

Rupture properties of the 2020 M_w 6.8 Calama (northern Chile) intraslab earthquake. Comparison with similar intraslab events in the region

Carlos Herrera,[1] Francisco Pastén-Araya,[2,3] Leoncio Cabrera,[4] Bertrand Potin,[2] Efraín Rivera,[3] Sergio Ruiz,[2] Raúl Madariaga[2] and Eduardo Contreras-Reyes[2]

[1] *Onur Seemann Consulting, Inc., Victoria, BC, V8P 4K1, Canada. E-mail: carlos@onurseemann.com*
[2] *Departamento de Geofísica, Facultad de Ciencias Físicas y Matemáticas, Universidad de Chile, Santiago 8370449, Chile*
[3] *Departamento de Obras Civiles, Facultad de Ciencias de la Ingeniería, Universidad Católica del Maule, Talca 3480112, Chile*
[4] *ISTerre Institut des Sciences de la Terre, CNRS, Université Grenoble Alpes, Grenoble 38058, France*

Accepted 2022 November 1. Received 2022 October 28; in original form 2022 February 11

SUMMARY

We study the 2020 M_w 6.8 Calama earthquake sequence that occurred within the subducting oceanic Nazca plate. The main shock is modelled via waveform inversion using a dynamic rupture model, while detection and location techniques are used to better characterize its aftershock sequence. We analyse the local seismotectonic and thermal context of the subducting Nazca plate to understand the trigger mechanism of this earthquake and how it compares with other significant earthquakes in the vicinity. The stress drop and the related dynamic rupture parameters of the Calama main shock are similar to those of the nearby 2007 M_w 6.8 Michilla and 2015 M_w 6.7 Jujuy intraslab earthquakes, which occurred to the west (trenchwards) and to the east (under the backarc) of the Calama earthquake, respectively. The sequences of these three events were located using a 3-D tomographic velocity model. While the Michilla earthquake sequence occurred within the oceanic crust at temperatures of ∼250 °C, the Calama sequence occurred within the upper lithospheric mantle at ∼350 °C and exhibited a smaller aftershock productivity than Michilla. Additionally, the 3-D tomographic model shows intermediate V_P/V_S ratios (1.72–1.76) in the region of the Calama earthquake. This indicates a less hydrated environment that could be responsible for the smaller aftershock productivity of the Calama earthquake.

Key words: Earthquake dynamics; Earthquake source observations; Seismicity and tectonics; Seismic tomography.

1 INTRODUCTION

Seismicity within the subducting oceanic Nazca plate in the central Andes occurs at a wide range of depths and magnitudes. Intraslab earthquakes in this region can be as shallow as ∼40 km depth, defining a deeper plane of seismicity aligned parallel to the plate interface in northern Chile (Bloch *et al.* 2014; Sippl *et al.* 2018). At depths greater than 60 km, the lack of coupling on the plate interface results in a considerable decrease of thrust earthquakes, and only intraslab earthquakes occur, defining a double seismic layer within the Nazca plate that extends to ∼140 km depth (Comte *et al.* 1999; Dorbath *et al.* 2008; Sippl *et al.* 2018; Florez & Prieto 2019; Lu *et al.* 2021). Beyond those depths, intraslab earthquakes are less frequent and more pervasively distributed within the subducting plate. Most of the recorded $M_w > 7.0$ intraslab events in this subduction zone have been deep focus earthquakes within the 550 and 650 km depth range, including the 1921–1922 earthquakes in northern Peru (Okal & Bina 1994), the 1994 Bolivia earthquake (Kikuchi & Kanamori 1994), and the 2015 earthquake doublets in the Peru–Brazil border (Ruiz *et al.* 2017). The shallower section of the Nazca plate in the central Andes has also ruptured with large intraslab earthquakes, such as the 1950 M_S 8.0 Antofagasta and 2005 M_W 7.8 Tarapacá earthquakes (Kausel & Campos 1992; Peyrat *et al.* 2006). Additionally, starting in 2007 and within a period of eight years, two $M_W > 6.5$ intraslab earthquakes struck at 40 and 250 km depth along the −23° parallel (Ruiz & Madariaga 2011; Herrera *et al.* 2017).

In this work, we study the rupture properties of a third intraslab event that occurred along the same −23° parallel: the 2020 M_W 6.8 Calama intraslab earthquake (Fig. 1). Considering the peculiar spatiotemporal distribution of these three major intraslab earthquakes, we compare their main shock properties and aftershock sequences, discussing them within the seismological, thermal and compositional context within the Nazca plate at latitude −23° in the central

© The Author(s) 2022. Published by Oxford University Press on behalf of The Royal Astronomical Society.

Downloaded from https://academic.oup.com/gji/article/232/3/2070/6795288 by CNRS user on 11 May 2023

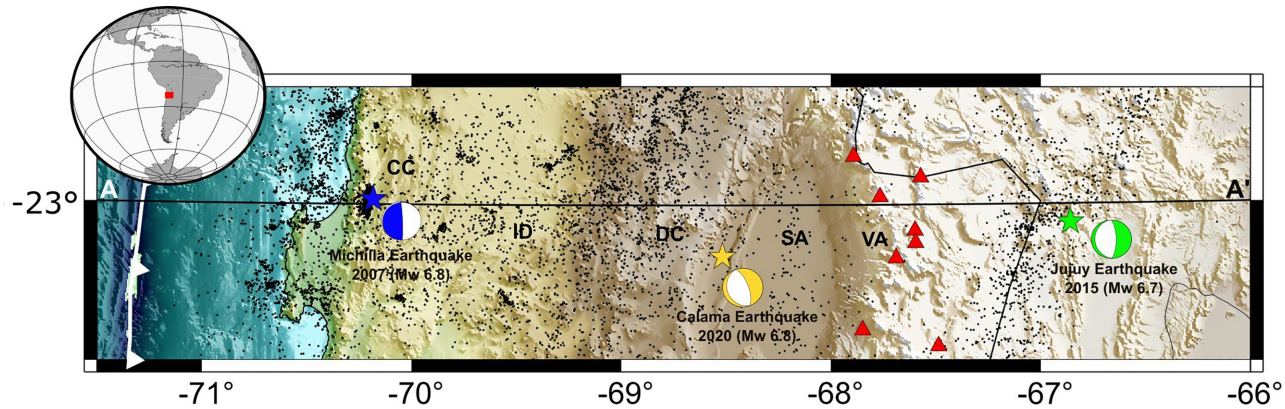

Figure 1. Seismological context of the Calama earthquake. Stars show the epicenters of the Michilla, Calama and Jujuy earthquakes. Their focal mechanisms from the GCMT catalogue (Dziewonski *et al.* 1981; Ekström *et al.* 2012) are also shown. The black dots indicate background seismicity reported by the CSN and relocated by Pastén-Araya *et al.* (2018). CC**:** Coastal Cordillera, ID**:** Intermediate Depression, DC**:** Domeyko Cordillera, SA**:** Salar of Atacama and VA**:** Volcanic arc. The red triangles correspond to the main active volcanoes. Cross-section A–A' runs along the − 23° parallel.

Andes. Our aim is to evaluate how these factors could control the main shock and aftershock characteristics of these events.

2 THE CALAMA EARTHQUAKE SEQUENCE

The Calama main shock occurred within the subducting Nazca plate at 123 km depth on 2020 June 3. Its epicentre was located at latitude −23.247° and longitude −68.53°, near the city of Calama in northern Chile, as reported by the Centro Sismológico Nacional (CSN) of the Universidad de Chile. The focal mechanism solution reported by the Global Centroid Moment Tensor (GCMT) catalogue (Dziewonski *et al.* 1981; Ekström *et al.* 2012) shows that the rupture occurred on a normal fault (see Fig. 1).

Several local seismic stations were operational at the time of the Calama earthquake. To carry out all the analyses shown in this work, we used strong motion and broad-band waveforms from multiparametric stations of the Integrated Plate boundary Observatory Chile network (IPOC, GFZ & CNRS-INSU 2006) and the CSN Network (Barrientos & National Seismological Center (CSN) Team 2018). Strong motion waveforms from the network of earthquake-triggered accelerometers of the CSN (Barrientos & National Seismological Center (CSN) Team 2018) were also used.

2.1 Earthquake detection and location

2.1.1 Earthquake detection using template matching

We used template matching (Gibbons & Ringdal 2006) to detect unreported earthquakes around the Calama main shock. This was done by analysing continuous broad-band velocity waveforms of nine stations from the IPOC and CSN networks situated near the epicentre (Fig. S1a, Supporting Information). We used the three components of these stations and bandpass filtered the data from 5 to 30 Hz, because this frequency range exhibits better signal-to-noise ratios (Cabrera *et al.* 2021). The template events are earthquakes reported by the CSN that occurred within a defined space–time window around the Calama earthquake. When defining a space–time window, a large window might allow the inclusion of additional events, but also more background seismicity that may not be related to the target sequence. By contrast, a smaller window mitigates this effect, but it is more susceptible to miss some events (e.g. Dascher-Cousineau *et al.* 2020; Cabrera *et al.* 2021). To determine the size of the region enclosing the seismicity of the Calama sequence, we followed the expression proposed by Dascher-Cousineau *et al.* (2020) based on the source radius estimated by Wells & Coppersmith (1994), resulting in a radius of 21 km around the hypocentre. In terms of time, we scanned the waveforms from one month before to one month after the main shock (between 2020 May 3 and July 3), since this is the maximum number of days for which the nine stations were operating continuously. This space–time window comprises the main shock and other 25 earthquakes that occurred after (Data set S1, Supporting Information). The waveforms of each template event were extracted by cutting the continuous data 0.5 s before the *P*-wave arrival and 5 s after the *S*-wave arrival. Wave arrivals were estimated using a local 1-D velocity model (Husen *et al.* 1999). The length of templates was defined in this way due to the difficulty of estimating *P*-wave arrivals accurately, given the limitations of the 1-D velocity model (e.g. Frank *et al.* 2017; Cabrera *et al.* 2021). To avoid detection of distant events not related to the studied sequence, correlation coefficients between the template waveforms and the continuous data were calculated within a sliding window that preserves the seismic moveouts using the Fast Matched Algorithm (Beaucé *et al.* 2018) and a GPU-architecture. This resulted in time-series that represent the similarity of the continuous data with every single template. We used a daily detection threshold that is 12 times the median absolute deviation (MAD) of the correlation function, which was averaged over all stations and channels to define the detection of an earthquake significantly similar to the template. The events detected with this criterion are assumed to occur at the same hypocentral location as their template (determined by the CSN). Their magnitudes were estimated by computing the median amplitude ratio between the template event and the aftershock over the considered stations, assuming that a tenfold increase in amplitude corresponds to one unit increase in magnitude (Peng & Zhao 2009). The resulting earthquake data set of the Calama sequence now includes 108 events in the magnitude range of 0.8–6.8, including templates (Data set S2, Supporting Information). Fig. S1b (Supporting Information) shows the comparison of the frequency–magnitude diagrams between the initial catalogue and the new catalogue. A higher number of event detections is now observed for the $M <$ ∼3.5 range, which is the completeness magnitude of the CSN catalogue (Barrientos & National Seismological Center (CSN) Team

Downloaded from https://academic.oup.com/gji/article/232/3/2070/6795288 by CNRS user on 11 May 2023

2018). Fig. S1c (Supporting Information) summarizes the normalized waveforms of all the events in the new catalogue recorded at station AF01, which is the closest to the epicentre (see Fig. S1a, Supporting Information). No earthquakes were detected before the main shock. The new catalogue of the Calama sequence features only aftershocks (see Fig. S1d, Supporting Information).

2.1.2 Location of the main shock and aftershocks

To obtain a better resolution of the possible fault plane, we carried out a location of the main shock and its aftershocks from the data set of 108 earthquakes that resulted from the template matching. The location was performed using the same stations that were used for template matching (Fig. S1a). First, the arrival times of the *P* and *S* waves were manually picked using the SEISAN software (Havskov & Ottemöller 1999). Once the arrival times were determined, the location was performed using the LocIn software (Potin 2016) on a regional 3-D tomographic velocity model (Contreras-Reyes *et al.* 2021; Pastén-Araya *et al.* 2021) (Fig. 2). Out of the 108 earthquakes, only the main shock and 37 aftershocks could be reliably located (Data set S3, Supporting Information) due to high noise level in the waveforms and limitations on station coverage. Location results indicate that the hypocentre of the Calama main shock occurred at 113 km depth. Aftershocks were located mostly updip from the hypocentre, between 100 and 113 km deep, defining a subvertical rupture plane, consistent with the NE dipping fault plane (strike = 333°; dip = 60° and rake = −91°) of the GCMT focal mechanism (Figs 1 and 2).

The same location method was applied for both the 2007 M_W 6.8 Michilla and 2015 M_W 6.7 Jujuy sequences, whose main shock depths were previously reported at 43 and 254 km, respectively (Ruiz & Madariaga 2011; Herrera *et al.* 2017; Pastén-Araya *et al.* 2018). Our location results show main shock hypocentral depths of 43 km for Michilla and 228 km for Jujuy. Compared with the Michilla earthquake, location uncertainties are larger for the Calama and Jujuy events, since they occurred at greater depths and were located with a smaller number of available stations, with important azimuthal gaps (Table 1 and Fig. S2a, Supporting Information). The located aftershock sequences of the Michilla and Jujuy earthquakes exhibit nearly vertical spatial distributions, closely aligned with the orientations of the steeper east-dipping fault planes of their respective focal mechanisms (Figs 1 and 2). These results are consistent with the previously reported aftershock distributions and selected fault planes for these two earthquakes. Additionally, we carried out a relocation of these events using a double-difference method. Although double-difference relocations tend to be slightly deeper (< 2 km) and slightly more clustered (Fig. S2b, Supporting Information), results are similar to the trends obtained with the absolute location approach.

2.2 The Calama main shock

Strong motion data were used to analyse both the ground shaking characteristics of the Calama main shock and its rupture properties. This earthquake generated a maximum peak ground acceleration (PGA) of 0.13 g at the closest station (hypocentral distance of 132 km). In general, the observed ground shaking intensities are within the ranges predicted by current ground motion models for Chilean intraslab earthquakes (see Text S1 and Fig. S3, Supporting Information). The low-frequency rupture properties of the main shock were inferred via inversion using a finite-fault model. Following the method used to model the Michilla and Jujuy earthquakes (Ruiz & Madariaga 2011; Herrera *et al.* 2017), the rupture model used in this work assumes an elliptical coseismic slip distribution with semi-axes a and b, centred at (x_0, y_0) within the fault plane. This ellipse is also allowed to rotate around its centre. The rupture nucleates at the hypocentre within a circular area. The overall rupture propagation in this model is controlled by a slip-weakening friction law (Ida 1972). This allows the determination of dynamic rupture parameters, such as: stress drop (T_e), yield stress (T_μ), slip-weakening distance (D_c) and a nucleation of radius R' with a stress T'_μ acting inside it (Madariaga & Ruiz 2016). The finite fault was centered at the hypocentre and was oriented using the strike, dip and rake of the NE-dipping plane of the focal mechanism reported by GCMT, as suggested by the spatial distribution of the located aftershocks. Prior to inversion, the baseline-corrected acceleration waveforms were integrated to velocity and filtered between 0.02 and 0.1 Hz with a Butterworth bandpass filter. Finally, the horizontal channels were rotated into radial and transverse components. To create the modelled waveforms, the wave propagation was simulated with the AXITRA code (Bouchon 1981; Coutant 1989) based on a 1-D velocity model (Husen *et al.* 1999). The inversion was performed using the Neighborhood Algorithm (Sambridge 1999), which in this case minimizes the misfit (χ^2) to find the best fitting model:

$$\chi^2 = \frac{\sum_i \left(\mathrm{obs}_i - \mathrm{pred}_i\right)^2}{\sum_i \mathrm{obs}_i^2}$$

which runs over the samples i of the observed (obs_i) and predicted (pred_i) waveforms. The three components (radial, transverse and vertical) were used in the inversion.

Due to the limitations of the 1-D velocity model, waveforms from a subset of eight stations around the epicentre were used for modelling (stations shown in Fig. 3a). The Neighborhood Algorithm converged towards a best dynamic rupture model that has a maximum coseismic slip of 1.59 m. The two axes of this elliptical model are 14.1 and 24.4 km long (Fig. 3a), with a rupture time of 5.6 s. Dynamically, the overall rupture had a $T_e =$ 10.1 MPa and $T_\mu =$ 11.9 MPa, nucleating within a circle of $R' =$ 1.46 km with $T'_\mu =$ 15.4 MPa inside. A distance $D_c =$ 0.7 m was required to nucleate the rupture. The model parameters started to converge towards these optimal values roughly after 10 000 sampled models (Fig. S4, Supporting Information). Fig. S5 (Supporting Information) shows the distributions and optimal values of these parameters. Some model parameters (e.g. b, y_0, T_e, T'_μ and D_c) are less Gaussian distributed than others, which could indicate trade-offs between them. In particular, the correlation is stronger between the stresses (Fig. S6, Supporting Information), since in the model formulation, T_μ and T'_μ depend on T_e. D_c also has a trade-off with T_μ in the friction formulation (Madariaga & Ruiz 2016, see also Fig. S6, Supporting Information), which is a contributing factor for the observed trend of D_c in Fig. S4 (Supporting Information), in addition to the resolution limitations of the parameter search grid. If the full seismograms are considered, the overall misfit associated to the best dynamic model is 0.58. In this case, the high-amplitude *SV* waves in the radial and vertical components could not be properly modelled in some stations (Fig. 3b, Supporting Information), resulting in this large misfit. This is likely due to converted body and surface

Downloaded from https://academic.oup.com/gji/article/232/3/2070/6795288 by CNRS user on 11 May 2023

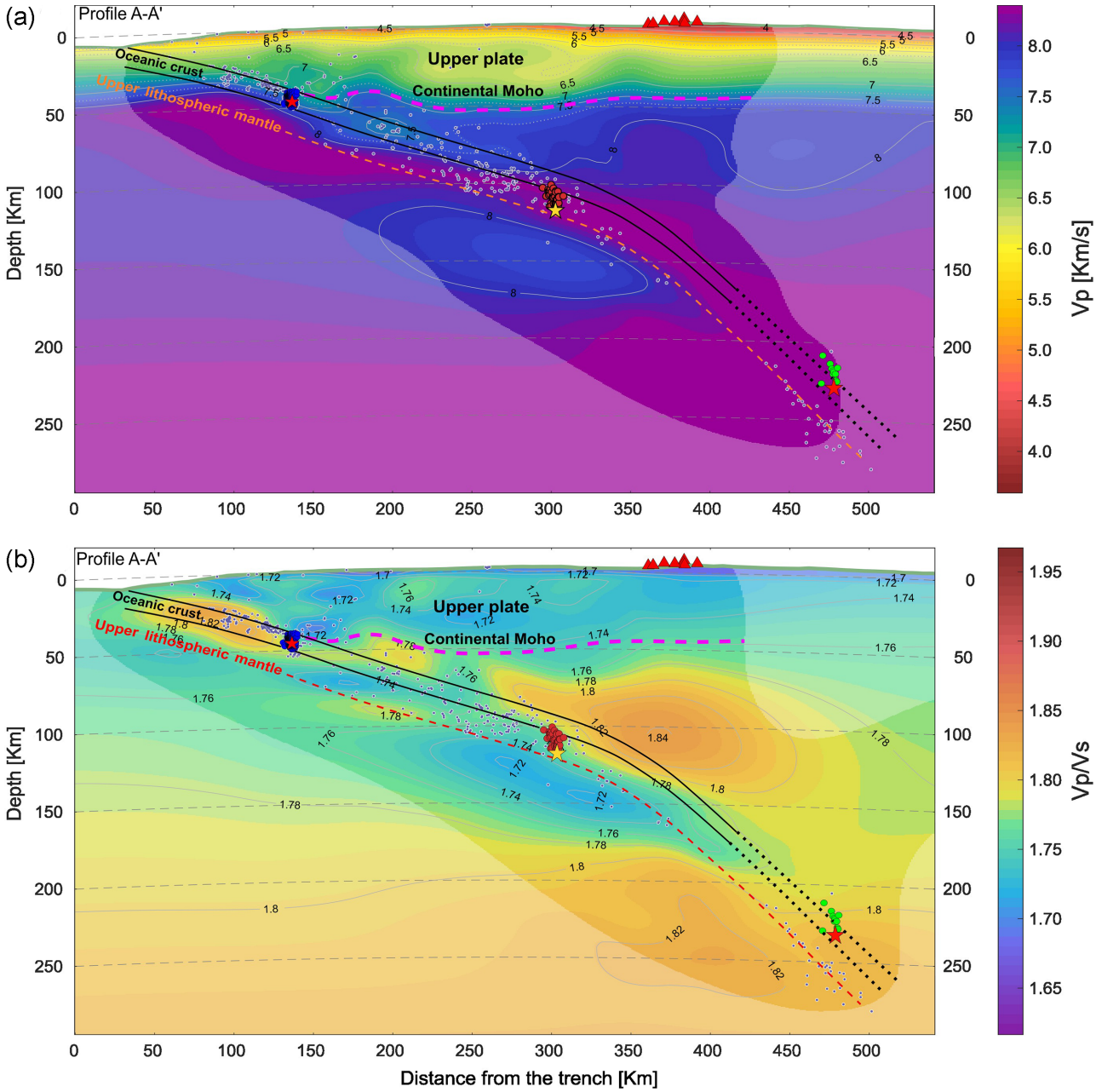

Figure 2. Seismicity within the 3-D tomographic model. (a) V_P and (b) V_P/V_S tomography models (Pastén-Araya *et al.* 2021) along cross-section A–A' of Fig. 1. Hypocentres of the Calama main shock and its aftershocks are shown with a yellow star and red circles, respectively. Red stars indicate the hypocentres of the Michilla and Jujuy earthquakes, and their aftershocks are shown with blue and green circles, respectively. The continental Moho was inferred by Tassara & Echaurren (2012). The plate interface as defined by Hayes *et al.* (2018) is shown by the continuous black line. The oceanic Moho defining the low limit of the oceanic crust was inferred by Contreras-Reyes *et al.* (2021). The oceanic crust is not accurately resolved below certain depths (segmented line extensions). The upper lithospheric mantle was defined based on the lower plane of seismicity reported by Sippl *et al.* (2018). Red triangles show the main active volcanoes. The discoloured areas of the tomographic model are regions of lower resolution.

waves arriving behind the *SV* waves, which could be generated by structures that are not represented by a simple 1-D velocity model. A similar case was shown by Herrera *et al.* (2017) for the Jujuy earthquake that occurred further east. Following their formulation, if the misfit is calculated using only *P* and high-amplitude *SH* waves (highlighted seismogram sections in Fig. 3b), its value is reduced to 0.24. This is the misfit formulation that was minimized in the inversion to obtain the described best dynamic model of the Calama earthquake.

3 DISCUSSION

3.1 Comparing dynamic properties of main shock ruptures

The Calama main shock was modelled using a finite-fault model, where the rupture propagation is controlled by a slip-weakening friction law. The other two main shocks at Michilla and Jujuy were previously modelled using the same dynamic rupture model and inversion method (Ruiz & Madariaga 2011; Herrera *et al.* 2017). This

Downloaded from https://academic.oup.com/gji/article/232/3/2070/6795288 by CNRS user on 11 May 2023

Table 1. Location of the Michilla, Calama and Jujuy earthquakes. These hypocentres were inferred in this work based on a 3-D velocity model. Their absolute errors were estimated based on the 90 per cent confidence level.

Event	Origin time	Lon. (°)	Lat. (°)	Depth (km)	RMS (s)	No. of stations	Azimuthal gap (°)	Horizontal error (km)	Vertical error (km)
Michilla	2007-12-16 08:09:17.28	−70.1828	−22.9962	43.5	0.05	24	81	2.5	3.0
Calama	2020-06-03 07:35:34.82	−68.5173	−23.2502	113.4	0.73	9	174	8.0	12.0
Jujuy	2015-02-11 18:57:20.3	−66.8584	−23.0936	228.7	0.8	13	193	9.0	14.0

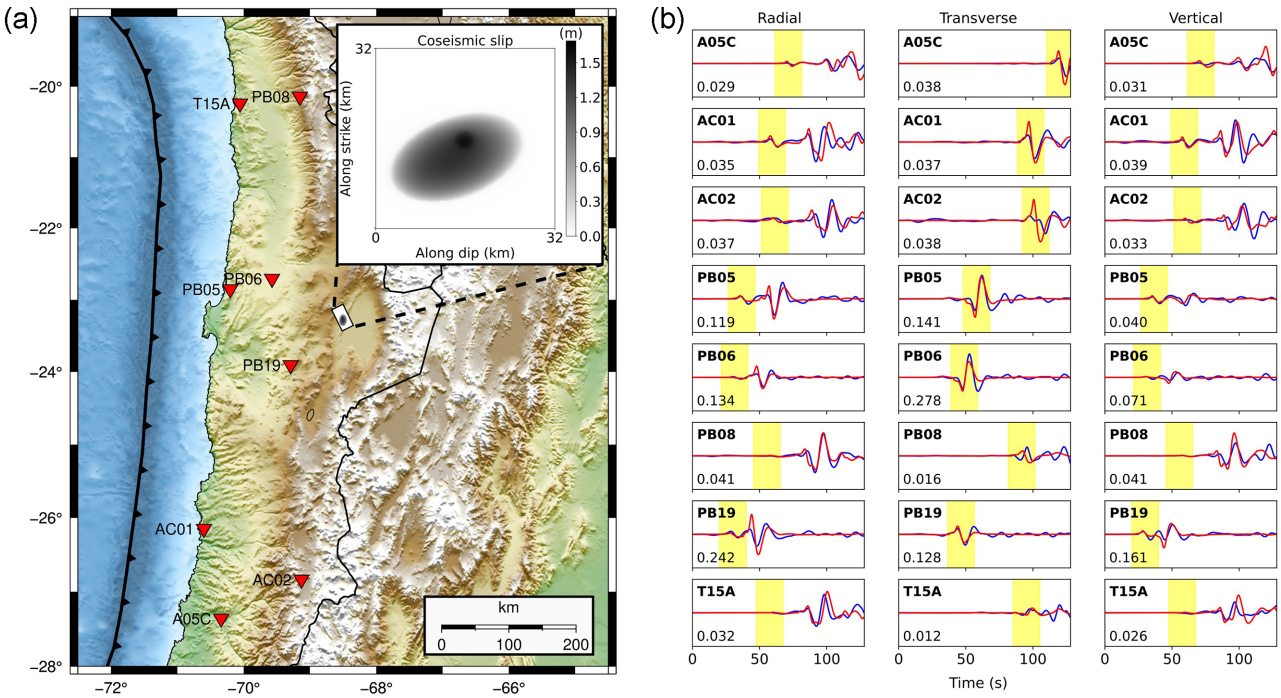

Figure 3. Dynamic modelling of the Calama earthquake. (a) Map showing the stations used for the modelling. The inset plot shows the best coseismic slip distribution of the Calama earthquake, zoomed from its epicentral location. (b) Observed (blue) and predicted (red) waveforms associated to the best dynamic model. Sections highlighted in yellow comprise the *P* waves (radial and vertical components) and *SH* waves (transverse component). The number within each plot is the maximum waveform amplitude (m s^{-1}).

allows a comparison of the inferred dynamic parameters with no bias related to differences in methods. The dynamic rupture parameters are summarized in Table 2, including the similarity parameter κ (Madariaga & Olsen 2000), calculated assuming the characteristic rupture size as the average of the ellipse semi-axes. All dynamic parameters of these three earthquakes are rather similar. In particular, the stress drop does not seem to be correlated with depth, which has also been observed with global earthquake databases (Poli & Prieto 2016). Overall, the T_e values of these three events fall within the empirically estimated ranges for intraslab earthquakes globally (e.g. Kanamori & Anderson 1975; Poli & Prieto 2016), and they are larger than the T_e values of thrust earthquakes inferred with the same method in northern Chile (Otarola *et al.* 2021).

3.2 The Calama earthquake occurrence within the upper lithospheric mantle

Intraslab earthquakes mostly occur in double seismic zones (DSZ), which have been observed in different subduction zones (Brudzinski *et al.* 2007). This DSZ is characterized by an upper seismicity plane (USP) located in the oceanic crust and a lower seismicity plane (LSP) located 20–40 km below the USP in the upper lithospheric mantle. The subduction zone of northern Chile is not an exception, and this DSZ has also been recognized in that region (Comte *et al.* 1999; Rietbrock & Waldhauser 2004; Bloch *et al.* 2014; Sippl *et al.* 2018; Florez & Prieto 2019; Lu *et al.* 2021). For example, the main shock and aftershocks of the Calama sequence located in this work are concentrated between 100 and 113 km depth, indicating that the rupture occurred in the LSP within the oceanic lithospheric mantle, below the oceanic Moho (Fig. 4). In contrast, the location results of the Michilla sequence indicate that its rupture occurred in the USP within the oceanic crust (Fig. 4).

Different mechanisms have been proposed for the generation of intraslab seismicity (e.g. Frohlich 2006; Houston 2015). For the seismicity located in the USP within the oceanic crust, there is a consensus that it could be related to the presence of fluids linked to dehydration processes within the oceanic crust at different pressures and temperatures (e.g. Kirby 1995; Hacker *et al.* 2003). Dehydration might cause the reduction of the effective normal stress, promoting brittle rupture of structures inherited from the faulting process in

Downloaded from https://academic.oup.com/gji/article/232/3/2070/6795288 by CNRS user on 11 May 2023

Table 2. Comparison of the best dynamic models of the Michilla, Calama and Jujuy earthquakes. For the Calama earthquake, values of their posterior mean and standard deviation are also shown in parenthesis.

Parameter	Michilla	Calama	Jujuy
Semi-axis a (km)	4.0	7.08 (7.05 ± 0.04)	7.94
Semi-axis b (km)	10.12	12.21 (12.24 ± 0.05)	4.87
Centre x_0 (km)	0.85	12.83 (12.95 ± 0.1)	12.71
Centre y_0 (km)	-2.0	14.56 (14.82 ± 0.26)	11.63
Rotation angle (°)	85.9	159.8 (162 ± 1.8)	203.4
T_e (MPa)	14.97	10.05 (9.86 ± 0.14)	11.87
T_μ (MPa)	19.18	11.87 (11.81 ± 0.12)	14.37
T'_μ (MPa)	23.65	15.35 (15.11 ± 0.25)	16.1
R' (km)	0.98	1.46 (1.47 ± 0.01)	1.09
D_c (m)	0.65	0.7 (0.67 ± 0.02)	0.41
κ	2.08	1.5 (1.53 ± 0.02)	1.97

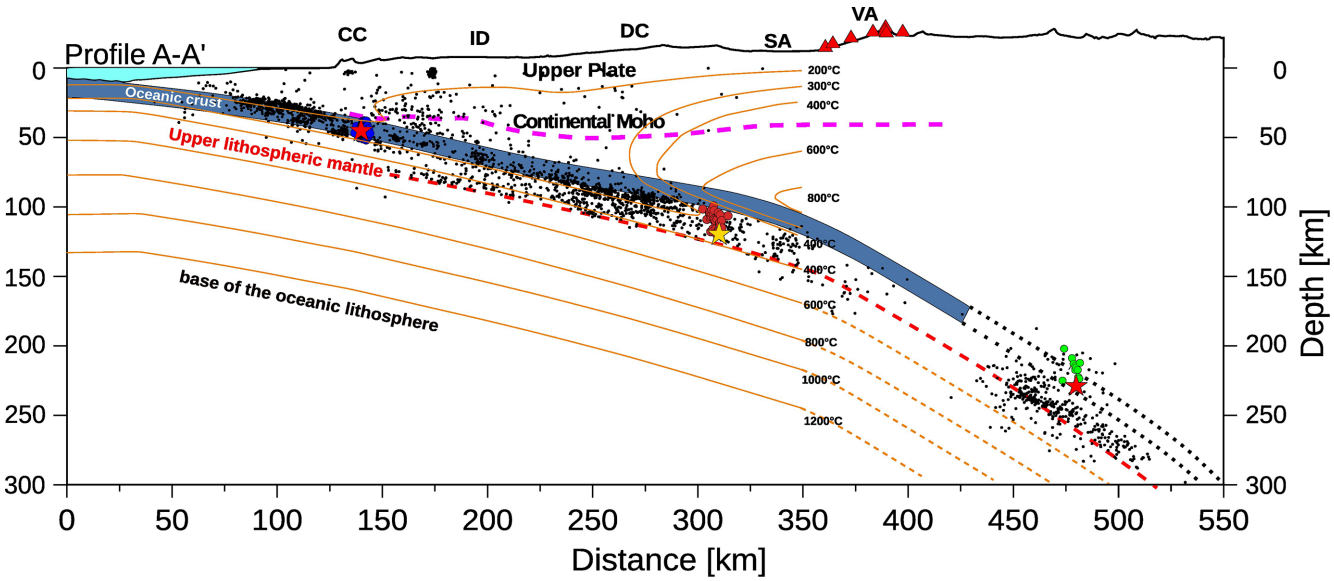

Figure 4. Cross-section A–A'. Symbols of the Michilla, Calama and Jujuy earthquakes and their aftershocks are as described in Fig. 2. The black dots indicate the background seismicity reported by the CSN and by Pastén-Araya *et al.* (2018). The continental Moho was inferred by Tassara & Echaurren (2012). The orange isotherms correspond to the thermal model of northern Chile (Cabrera *et al.* 2021). The slab geometry is the Slab2.0 (Hayes *et al.* 2018). The oceanic crust and isotherms are not accurately resolved below certain depths (segmented line extensions). CC: Coastal Cordillera, ID: Intermediate Depression, DC: Domeyko Cordillera, SA: Salar of Atacama and VA: Volcanic arc. The red triangles correspond to the main active volcanoes. The base of the oceanic lithosphere at ∼1200 °C is based on Richards *et al.* (2018).

the outer-rise zone prior to subduction (Ranero *et al.* 2005; Ruiz & Contreras-Reyes 2015; Pastén-Araya *et al.* 2018; Cabrera *et al.* 2021). However, the mechanisms that generate intraslab seismicity in the LSP are still a subject of debate (Duesterhoeft *et al.* 2014; Ferrand *et al.* 2017; Ohuchi *et al.* 2017; Scambelluri *et al.* 2017). Mechanisms that point to a hydrated lithospheric oceanic mantle have been proposed to trigger seismicity in the LSP (Bloch *et al.* 2018; Cai *et al.* 2018). On the other hand, analysis of laboratory and field data suggests that faulting could be triggered in dry rocks within a partially hydrated oceanic lithospheric mantle (Ferrand *et al.* 2017; Kita & Ferrand 2018). This process has been referred to as dehydration-driven stress transfer, which would not require the presence of a highly hydrated lithospheric mantle. Instead, a rupture could nucleate in a weakly hydrated portion of the lithosphere and propagate to dry regions of the lithosphere due to the stress transfer associated with volumetric change of the rock. Additionally, Florez & Prieto (2019) found that globally, LSP seismicity has consistently smaller b-values compared with the USP seismicity, which would also indicate a relatively dry environment in the LSP.

According to hydrological and numerical models, dehydration of the subducted slab occurs mainly in three stages (Ulmer & Trommsdorff 1995; Peacock 2001; Hacker *et al.* 2003; Rüpke *et al.* 2004). First, dewatering of subducting sediments leads to hydration of the mantle wedge at depths < 20 km (ANCORP Working Group 1999; Rüpke *et al.* 2004). Second, metamorphic dehydration reactions of the subducting oceanic crust increase pore pressure and decrease effective confining pressure, thereby promoting intraslab seismicity (60–80 km depth, Peacock 2001; Hacker *et al.* 2003). Third, at depths larger than 100 km, the subducting lithospheric mantle dehydrates (Rüpke *et al.* 2004) and triggers intraslab seismicity (Yuan *et al.* 2000; Peacock 2001) causing partial melting and leading to arc volcanism (Rüpke *et al.* 2004; Contreras-Reyes *et al.* 2021). In our study case, dehydration reactions of the upper lithospheric mantle are consistent with a zone of intermediate V_P/V_S ratios (1.72–1.76) in the region of the Calama earthquake (Fig. 2b). This zone also presents 'typical' uppermost mantle V_P values of ∼8.3 km s^{-1} (Fig. 2a) at > 600 MPa, suggesting the presence of dry dunite/peridotite mantle rocks (Christensen 1996). In addition,

Downloaded from https://academic.oup.com/gji/article/232/3/2070/6795288 by CNRS user on 11 May 2023

the mantle wedge presents large V_P/V_S ratios of 1.8–1.84 above the location of the Calama earthquake, which indirectly indicates the occurrence of massive dehydration reactions from the subducting oceanic lithosphere (e.g. Rüpke *et al.* 2004).

In summary, our results indicate that the Calama earthquake is likely a good example of an event triggered by the dehydration-driven stress transfer mechanism in dryer conditions. By contrast, the Michilla earthquake occurred within the oceanic crust where $V_P/V_S > 1.8$ (Fig. 2b), suggesting that the presence of fluids and a reduction of the effective normal stress could favour earthquake occurrence. The oceanic crust cannot be resolved in the region of the Jujuy earthquake. Moreover, the tomographic model cannot resolve V_P/V_S properly beyond 150–180 depth (Fig. 2b). Therefore, considering this and the location uncertainties of the Jujuy earthquake (see Table 1 and Fig. S2, Supporting Information), for now the available data shows that this event occurred somewhere within the uppermost oceanic lithosphere, likely at lithostatic pressures of about 7 GPa and estimated temperatures of 300–600 °C (Fig. 4). At these *P*–*T* conditions, the uppermost oceanic/subducting lithosphere dehydrates, favouring brittle faulting (Rüpke *et al.* 2004).

3.3 Thermal conditions and aftershock rate

Several studies have suggested that temperature could be an important factor that controls the distribution of both thrust and intraslab seismicity (Oleskevich *et al.* 1999; Wang *et al.* 2015; Wei *et al.* 2017; Liu *et al.* 2021). To try to establish the degree of influence of temperature on the Calama sequence, as well as on the other two intraslab earthquakes, we used the thermal model of northern Chile proposed by Cabrera *et al.* (2021), which is well defined between the trench and the volcanic arc in the upper ∼200 km (Fig. 4). Clear common trends are observed between the isotherms and the seismicity distribution. While the thrust seismicity is concentrated along the 200 °C isotherm, the intraslab seismicity defined by the DZS is mostly concentrated between the 300 and 400 °C isotherms. A decrease in the seismicity is observed at higher temperatures, which could indicate a transition from brittle to ductile behaviour at greater depths below the 500–600 °C isotherm along the subducting plate, particularly in the zones of the Michilla and Calama earthquakes. The brittle/ductile transition in the region of the Jujuy event seems to be deeper across the 600–800 °C isotherms (Fig. 4). Cabrera *et al.* (2021) studied intermediate-depth seismicity in northern Chile between latitudes −18° and −20° (200–300 km northwards of our study area) and concluded that the neutral surface and brittle/ductile transition zone becomes deeper within the subducting plate at depths of 80–120 km (600–800 °C). Seismicity in the region of the Jujuy sequence seems to be consistent with these findings (Fig. 4).

The Calama sequence occurred between the 300 and 400 °C isotherms (Fig. 4), and its aftershocks mostly occurred at shallower depths than the main shock. Similar trends were observed for the aftershock distributions of the 2019 M_W 6.7 Coquimbo and 2018 M_W 7.1 Anchorage intraslab earthquakes, which also exhibited shallower aftershocks than the main shock (Liu *et al.* 2019; Ruiz *et al.* 2019; Ruppert *et al.* 2020). In particular, the Coquimbo main shock occurred between the 600 and 700 °C isotherms within the subducting plate (Ruiz *et al.* 2019). However, its aftershocks mostly occurred at shallower (and colder) layers, at temperatures below 450 °C. These examples indicate that temperature could play a significant role in the aftershock distribution of intermediate-depth intraslab earthquakes, which tend to occur in layers of lower temperatures.

The aftershock productivity of intraslab earthquakes is another aspect that is related to both the zone where they are triggered and the temperature. Cabrera *et al.* (2021) carried out an analysis of several intraslab earthquakes in northern Chile, finding that intraslab earthquakes that occur at greater depths below the 400–450 °C isotherms produce very few or no aftershocks, and would be associated with a dry environment. Conversely, those events that occur at depths shallower than the 400–450 °C isotherms usually produce more aftershocks and would be associated with a more hydrated environment. Our results corroborate this observation, particularly when comparing the cases of the 2007 Michilla and the 2020 Calama earthquakes, which occurred at depths where the thermal model is still well defined. The Michilla earthquake occurred within the oceanic crust between the 200 and 300 °C isotherms (Fig. 4), producing a large number of aftershocks and a zone with persistent seismicity in time (Ruiz & Madariaga 2011; Fuenzalida *et al.* 2013; Pastén-Araya *et al.* 2018). Conversely, the Calama main shock and its aftershocks occurred in the upper lithospheric mantle between the 300 and 400 °C isotherms. Within the first five days after the main shock, the Calama earthquake produced a much smaller number of $M \geq 2.0$ aftershocks (53 events) compared with the Michilla earthquake (313 events). Therefore, these observations, in combination with the observed differences of V_P/V_S ratios between the Calama and Michilla earthquakes, suggest that the Calama earthquake occurred in a warmer and less hydrated environment than the Michilla earthquake, which could be responsible for its lower aftershock productivity. This is consistent with observations obtained by Chu & Beroza (2022) in the subducting Pacific Plate in Japan. They found that the aftershock productivity is correlated with V_P/V_S ratio, discussing that a high V_P/V_S ratio can be a result of high fluid pressure and a larger number of faults and cracks that could be fluid-filled, or also oriented perpendicular to ray paths.

4 CONCLUSIONS

The 2020 M_W 6.8 Calama earthquake is an intraslab earthquake that occurred at intermediate depths, at the same latitude (−23°) as the 2007 M_W 6.8 Michilla and 2015 M_W 6.7 Jujuy intraslab events. It featured ground shaking intensities that are typical of Chilean intraslab earthquakes.

The hypocentre of the Calama earthquake was located at 113 km depth using a 3-D model. The same method was used to locate the hypocentres of the Michilla and Jujuy earthquakes, resulting in depths of 43 and 228 km, respectively. At their located depths, we observed that the Michilla earthquake occurred within the oceanic crust, while the Calama earthquake occurred within the upper lithospheric mantle, below the oceanic crust. The resolution of our database does not allow exact interpretations of the Jujuy earthquake location within the uppermost oceanic lithosphere due to the larger uncertainties in earthquake, slab and oceanic Moho locations at those depths.

The dynamic properties of the Calama earthquake were inferred through modelling of low-frequency waveforms, which is the same method that was previously used to model the Michilla and Jujuy earthquakes. Despite their different hypocentral depths and locations in different layers of the subducting oceanic plate, the dynamic properties of these three events are similar. Particularly, their stress

Downloaded from https://academic.oup.com/gji/article/232/3/2070/6795288 by CNRS user on 11 May 2023

drop values range between 10 and 15 MPa, within the observed ranges of intraslab earthquakes, which are in general larger than the stress drop values of thrust earthquakes.

Thermal and pressure conditions of the subducting plate likely control the spatial distribution of intraslab seismicity along the -23° parallel in northern Chile, where the 500–600° C isotherms along the subducting plate define a limit for intraslab seismicity occurrence down to ∼150 km depth. Additionally, the varying water content and thermal conditions of mantle rocks in the areas where intraslab earthquakes occur play an important role in their aftershock productivity. For instance, the Michilla earthquake occurred within the oceanic crust at temperatures between 200 and 300° C, exhibiting a strong aftershock activity. The large V_P/V_S ratio (> 1.8) at that location indicates a more hydrated environment that favours brittle rupture and an increase in aftershocks. On the other hand, the Calama earthquake occurred in the uppermost lithospheric mantle, where the V_P/V_S ratio is smaller (between 1.72 and 1.76), and temperatures vary between 300 and 400° C. This earthquake exhibited a smaller aftershock productivity, which is likely a result of a less hydrated environment, as suggested by the reduced V_P/V_S ratios in this region.

Our results show that even though the Michilla and Calama earthquakes occurred in regions of different thermal and compositional characteristics within the Nazca plate, curiously these factors do not significantly affect the dynamic characteristics of the main shocks, which were found to be within the typical ranges of intraslab events. However, they do affect their aftershock productivity. Additional studies with a larger database of well-recorded earthquakes are necessary to confirm if this trend is observed in more events.

ACKNOWLEDGMENTS

The author CH designed and wrote most of the manuscript. He also carried out the strong motion analysis and the dynamic modelling of the Calama main shock. FP-A designed and contributed with the discussion that relates the tomography and thermal models with the analysed earthquake sequences. FP-A and RM thank the Programa de Riesgo Sísmico (PRS) of the Universidad de Chile. LC carried out the template matching using the University of Grenoble Alpes (UGA) High-Performance Computing infrastructures CIMENT. He was supported by the European Union Horizon 2020 Research and Innovation Programme (grant agreements, 802777-MONIFAULTS). BP and ER contributed with the location and relocation analyses of the three studied earthquakes and their aftershocks. Part of the computations were performed using the GRICAD infrastructure (https://gricad.univ-grenoble-alpes.fr), which is supported by Grenoble research communities. SR, RM and EC-R contributed with editing assistance and review of the manuscript during preparation. EC-R also acknowledges the support of PIA/FONDEYT grant 1210101. We finally thank Jörg Renner, Frederik Tilmann and another anonymous reviewer for their thorough reviews that improved this work.

DATA AVAILABILITY

Waveform data from multiparametric stations were downloaded from the International Federation of Digital Seismograph Networks (FDSN) web services using the ObsPy toolkit (Beyreuther *et al.* 2010). Waveforms from the earthquake-triggered network of accelerometers of the CSN can be accessed from their website (evtdb.csn.uchile.cl). The earthquake catalogues used in this study can be accessed from their respective websites: CSN catalogue (www.sismologia.cl) and GCMT catalogue (www.globalcmt.org). Maps were created using Generic Mapping Tools (Wessel *et al.* 2013).

REFERENCES

ANCORP Working Group., 1999. Seismic reflection image revealing offset of Andean subduction-zone earthquake locations into oceanic mantle, *Nature,* **397**(6717), 341. https://doi.org/10.1038/16909.

Barrientos, S., & National Seismological Center (CSN) Team, 2018. The seismic network of Chile, *Seismol. Res. Lett.,* **89**(2A), 467–474.

Beaucé, E., Frank, W. B. & Romanenko, A., 2018. Fast matched filter (FMF): an efficient seismic matched-filter search for both CPU and GPU architectures, *Seismol. Res. Lett.,* **89**(1), 165–172.

Beyreuther, M., Barsch, R., Krischer, L., Megies, T., Behr, Y. & Wassermann, J., 2010. ObsPy: a Python toolbox for seismology, *Seismol. Res. Lett.,* **81**(3), 530–533.

Bloch, W., Kummerow, J., Salazar, P., Wigger, P. & Shapiro, S. A., 2014. High-resolution image of the North Chilean subduction zone: seismicity, reflectivity and fluids, *Geophys. J. Int.,* **197**(3), 1744–1749.

Bloch, W., John, T., Kummerow, J., Salazar, P., Krüger, O. S. & Shapiro, S. A., 2018. Watching dehydration: seismic indication for transient fluid pathways in the oceanic mantle of the subducting Nazca slab, *Geochem. Geophys. Geosyst.,* **19**(9), 3189–3207.

Bouchon, M., 1981. A simple method to calculate Green's functions for elastic layered media, *Bull. seism. Soc. Am.,* **71**(4), 959–971.

Brudzinski, M. R., Thurber, C. H., Hacker, B. R. & Engdahl, E. R., 2007. Global prevalence of double Benioff zones, *Science,* **316**(5830), 1472–1474.

Cabrera, L., Ruiz, S., Poli, P., Contreras-Reyes, E., Osses, A. & Mancini, R., 2021. Northern Chile intermediate-depth earthquakes controlled by plate hydration, *Geophys. J. Int.,* **226**(1), 78–90.

Cai, C., Wiens, D. A., Shen, W. & Eimer, M., 2018. Water input into the Mariana subduction zone estimated from ocean-bottom seismic data, *Nature,* **563**(7731), 389–392.

Christensen, N. I., 1996. Poisson's ratio and crustal seismology, *J. geophys. Res.: Solid Earth,* **101**(B2), 3139–3156.

Chu, S. X. & Beroza, G. C., 2022. Aftershock productivity of intermediate-depth earthquakes in Japan, *Geophys. J. Int.,* **230**(1), 448–463. .

Comte, D. *et al.*, 1999. A double-layered seismic zone in Arica, northern Chile, *Geophys. Res. Lett.,* **26**(13), 1965–1968.

Contreras-Reyes, E. *et al.*, 2021. Subduction zone fluids and arc magmas conducted by lithospheric deformed regions beneath the central Andes, *Sci. Rep.,* **11**(1), 1–12.

Coutant, O., 1989. *Programme de Simulation Numérique AXITRA, Rapport LGIT,* Universite Joseph Fourier, Grenoble, France.

Dascher-Cousineau, K., Brodsky, E. E., Lay, T. & Goebel, T. H., 2020. What controls variations in aftershock productivity?, *J. geophys. Res.: Solid Earth,* **125**(2), e2019JB018111. https://doi.org/10.1029/2019JB018111.

Dorbath, C., Gerbault, M., Carlier, G. & Guiraud, M., 2008. Double seismic zone of the Nazca plate in northern Chile: high-resolution velocity structure, petrological implications, and thermomechanical modeling, *Geochem. Geophys. Geosyst.,* **9**(7). https://doi.org/10.1029/2008GC002020.

Duesterhoeft, E., Quinteros, J., Oberhänsli, R., Bousquet, R. & de Capitani, C., 2014. Relative impact of mantle densification and eclogitization of slabs on subduction dynamics: a numerical thermodynamic/thermokinematic investigation of metamorphic density evolution, *Tectonophysics,* **637,** 20–29.

Dziewonski, A. M., Chou, T. A. & Woodhouse, J. H., 1981. Determination of earthquake source parameters from waveform data for studies of global and regional seismicity, *J. geophys. Res.: Solid Earth,* **86**(B4), 2825–2852.

Ekström, G., Nettles, M. & Dziewoński, A. M., 2012. The global CMT project 2004–2010: centroid-moment tensors for 13,017 earthquakes, *Phys. Earth planet. Inter.,* **200,** 1–9.

Downloaded from https://academic.oup.com/gji/article/232/3/2070/6795288 by CNRS user on 11 May 2023

Ferrand, T. P. *et al.*, 2017. Dehydration-driven stress transfer triggers intermediate-depth earthquakes, *Nat. Commun.,* **8**(1), 1–11.

Florez, M. A. & Prieto, G. A., 2019. Controlling factors of seismicity and geometry in double seismic zones, *Geophys. Res. Lett.,* **46**(8), 4174–4181.

Frank, W. B., Poli, P. & Perfettini, H., 2017. Mapping the rheology of the central Chile subduction zone with aftershocks, *Geophys. Res. Lett.,* **44**(11), 5374–5382.

Frohlich, C., 2006. *Deep Earthquakes*. Cambridge: Cambridge University Press. .

Fuenzalida, A., Schurr, B., Lancieri, M., Sobiesiak, M. & Madariaga, R., 2013. High-resolution relocation and mechanism of aftershocks of the 2007 Tocopilla (Chile) earthquake, *Geophys. J. Int.,* **194**(2), 1216–1228.

GFZ, & CNRS-INSU, 2006. IPOC Seismic Network, Integrated Plate boundary Observatory Chile – IPOC. Other/Seismic Network. https://doi.org/10.14470/PK615318.

Gibbons, S. J. & Ringdal, F., 2006. The detection of low magnitude seismic events using array-based waveform correlation, *Geophys. J. Int.,* **165**(1), 149–166.

Havskov, J. & Ottemöller, L., 1999. SeisAn earthquake analysis software, *Seismol. Res. Lett.,* **70**(5), 532–534.

Hacker, B. R., Peacock, S. M., Abers, G. A. & Holloway, S. D., 2003. Subduction factory 2. Are intermediate-depth earthquakes in subducting slabs linked to metamorphic dehydration reactions?, *J. geophys. Res.: Solid Earth,* **108**(B1). https://doi.org/10.1029/2001JB001129.

Hayes, G. P., Moore, G. L., Portner, D. E., Hearne, M., Flamme, H., Furtney, M. & Smoczyk, G. M., 2018. Slab2, a comprehensive subduction zone geometry model, *Science,* **362**(6410), 58–61.

Herrera, C., Ruiz, S., Madariaga, R. & Poli, P., 2017. Dynamic inversion of the 2015 Jujuy earthquake and similarity with other intraslab events, *Geophys. J. Int.,* **209**(2), 866–875.

Houston, H., 2015. Deep earthquakes, in *Treatise on Geophysics,* pp. 329–354, ed. Schubert, G., Elsevier.

Husen, S., Kissling, E., Flueh, E. & Asch, G., 1999. Accurate hypocentre determination in the seismogenic zone of the subducting Nazca Plate in northern Chile using a combined on-/offshore network, *Geophys. J. Int.,* **138**(3), 687–701.

Ida, Y., 1972. Cohesive force across the tip of a longitudinal-shear crack and Griffith's specific surface energy, *J. geophys. Res.,* **77**(20), 3796–3805.

Kanamori, H. & Anderson, D. L., 1975. Theoretical basis of some empirical relations in seismology, *Bull. seism. Soc. Am.,* **65**(5), 1073–1095.

Kausel, E. & Campos, J., 1992. The Ms = 8 tensional earthquake of 9 December 1950 of northern Chile and its relation to the seismic potential of the region, *Phys. Earth planet. Inter.,* **72**(3-4), 220–235.

Kikuchi, M. & Kanamori, H., 1994. The mechanism of the deep Bolivia earthquake of June 9, 1994, *Geophys. Res. Lett.,* **21**(22), 2341–2344.

Kirby, S., 1995. Interslab earthquakes and phase changes in subducting lithosphere, *Rev. Geophys.,* **33**(S1), 287–297.

Kita, S. & Ferrand, T. P., 2018. Physical mechanisms of oceanic mantle earthquakes: comparison of natural and experimental events, *Sci. Rep.,* **8**(1), 1–11.

Liu, C., Lay, T., Xie, Z. & Xiong, X., 2019. Intraslab deformation in the 30 November 2018 Anchorage, Alaska, MW 7.1 earthquake, *Geophys. Res. Lett.,* **46**(5), 2449–2457.

Liu, H., Gurnis, M., Leng, W., Jia, Z. & Zhan, Z., 2021. Tonga slab morphology and stress variations controlled by a relic slab: implications for deep earthquakes in the Tonga-Fiji Region, *Geophys. Res. Lett.,* **48**(7), e2020GL091331. https://doi.org/10.1029/2020GL091331.

Lu, P., Zhang, H., Gao, L. & Comte, D., 2021. Seismic imaging of the double seismic zone in the subducting slab in Northern Chile, *Earthq. Res. Adv.,* **1**(1), 100003. https://doi.org/10.1016/j.eqrea.2021.100003.

Madariaga, R. & Olsen, K., 2000. Criticality of rupture dynamics in 3-D, *Pure appl. Geophys.,* **157,** 1981–2001.

Madariaga, R. & Ruiz, S., 2016. Earthquake dynamics on circular faults: a review 1970–2015, *J. Seismol.,* **20**(4), 1235–1252.

Ohuchi, T., Lei, X., Ohfuji, H., Higo, Y., Tange, Y., Sakai, T., Fujino, K. & Irifune, T., 2017. Intermediate-depth earthquakes linked to localized heating in dunite and harzburgite, *Nat. Geosci.,* **10**(10), 771–776.

Okal, E. A. & Bina, C. R., 1994. The deep earthquakes of 1921–1922 in northern Peru, *Phys. Earth planet. Inter.,* **87**(1-2), 33–54.

Oleskevich, D. A., Hyndman, R. D. & Wang, K., 1999. The updip and downdip limits to great subduction earthquakes: thermal and structural models of Cascadia, south Alaska, SW Japan, and Chile, *J. geophys. Res.: Solid Earth,* **104**(B7), 14965–14991.

Otarola, C., Ruiz, S., Herrera, C., Madariaga, R. & Siegel, C., 2021. Dynamic rupture of subduction earthquakes located near the trench, *Earth planet. Sci. Lett.,* **562,** 116842. https://doi.org/10.1016/j.epsl.2021.116842.

Pastén-Araya, F. *et al.*, 2018. Fluids along the plate interface influencing the frictional regime of the Chilean subduction zone, northern Chile, *Geophys. Res. Lett.,* **45**(19), 10–378.

Pastén-Araya, F. *et al.*, 2021. Seismicity in the upper plate of the Northern Chilean offshore forearc: evidence of splay fault south of the Mejillones Peninsula, *Tectonophysics,* **800,** 228706. https://doi.org/10.1016/j.tecto.2020.228706.

Peacock, S. M., 2001. Are the lower planes of double seismic zones caused by serpentine dehydration in subducting oceanic mantle?, *Geology,* **29**(4), 299–302.

Peng, Z. & Zhao, P., 2009. Migration of early aftershocks following the 2004 Parkfield earthquake, *Nat. Geosci.,* **2**(12), 877–881.

Peyrat, S. *et al.*, 2006. Tarapacá intermediate-depth earthquake (Mw 7.7, 2005, northern Chile): a slab-pull event with horizontal fault plane constrained from seismologic and geodetic observations, *Geophys. Res. Lett.,* **33**(22). https://doi.org/10.1029/2006GL027710.

Poli, P. & Prieto, G. A., 2016. Global rupture parameters for deep and intermediate-depth earthquakes, *J. geophys. Res.: Solid Earth,* **121**(12), 8871–8887.

Potin, B., 2016. *Les Alpes Occidentales: Tomographie, Localisation de Séismes et Topographie du Moho,* Doctoral dissertation, Université Grenoble Alpes, Grenoble, France.

Ranero, C. R., Villaseñor, A., Phipps Morgan, J. & Weinrebe, W., 2005. Relationship between bend-faulting at trenches and intermediate-depth seismicity, *Geochem. Geophys. Geosyst.,* **6**(12). https://doi.org/10.1029/2005GC000997.

Richards, F. D., Hoggard, M. J., Cowton, L. R. & White, N. J., 2018. Reassessing the thermal structure of oceanic lithosphere with revised global inventories of basement depths and heat flow measurements, *J. geophys. Res.: Solid Earth,* **123**(10), 9136–9161.

Rietbrock, A. & Waldhauser, F., 2004. A narrowly spaced double-seismic zone in the subducting Nazca plate, *Geophys. Res. Lett.,* **31**(10). https://doi.org/10.1029/2005GC000997.

Ruiz, J. A. & Contreras-Reyes, E., 2015. Outer rise seismicity boosted by the Maule 2010 Mw 8.8 megathrust earthquake, *Tectonophysics,* **653,** 127–139.

Ruiz, S. & Madariaga, R., 2011. Determination of the friction law parameters of the Mw 6.7 Michilla earthquake in northern Chile by dynamic inversion, *Geophys. Res. Lett.,* **38**(9). https://doi.org/10.1029/2011GL047147.

Ruiz, S., Tavera, H., Poli, P., Herrera, C., Flores, C., Rivera, E. & Madariaga, R., 2017. The deep Peru 2015 doublet earthquakes, *Earth planet. Sci. Lett.,* **478,** 102–109.

Ruiz, S., Ammirati, J. B., Leyton, F., Cabrera, L., Potin, B. & Madariaga, R., 2019. The January 2019 (Mw 6.7) Coquimbo earthquake: insights from a seismic sequence within the Nazca plate, *Seismol. Res. Lett.,* **90**(5), 1836–1843.

Rüpke, L. H., Morgan, J. P., Hort, M. & Connolly, J. A., 2004. Serpentine and the subduction zone water cycle, *Earth planet. Sci. Lett.,* **223**(1-2), 17–34.

Ruppert, N. A., Nayak, A., Thurber, C. & Richards, C., 2020. Aftershock analysis of the 2018 M w 7.1 Anchorage, Alaska, earthquake: relocations and regional moment tensors, *Seismol. Res. Lett.,* **91**(1), 114–125.

Sambridge, M., 1999. Geophysical inversion with a neighbourhood algorithm—I. Searching a parameter space, *Geophys. J. Int.,* **138**(2), 479–494.

Scambelluri, M., Pennacchioni, G., Gilio, M., Bestmann, M., Plümper, O. & Nestola, F., 2017. Fossil intermediate-depth earthquakes in subducting slabs linked to differential stress release, *Nat. Geosci.,* **10**(12), 960–966.

Downloaded from https://academic.oup.com/gji/article/232/3/2070/6795288 by CNRS user on 11 May 2023

Sippl, C., Schurr, B., Asch, G. & Kummerow, J., 2018. Seismicity structure of the northern Chile forearc from >100,000 double-difference relocated hypocenters, *J. geophys. Res.: Solid Earth,* **123**(5), 4063–4087.

Tassara, A. & Echaurren, A., 2012. Anatomy of the Andean subduction zone: three-dimensional density model upgraded and compared against global-scale models, *Geophys. J. Int.,* **189**(1), 161–168.

Ulmer, P. & Trommsdorff, V., 1995. Serpentine stability to mantle depths and subduction-related magmatism, *Science,* **268**(5212), 858–861.

Wang, K., He, J., Schulzeck, F., Hyndman, R. D. & Riedel, M., 2015. Thermal condition of the 27 October 2012 Mw 7.8 Haida Gwaii subduction earthquake at the obliquely convergent queen charlotte margin, *Bull. seism. Soc. Am.,* **105**(2B), 1290–1300.

Wei, S. S., Wiens, D. A., van Keken, P. E. & Cai, C., 2017. Slab temperature controls on the Tonga double seismic zone and slab mantle dehydration, *Sci. Adv.,* **3**(1), e1601755. https://doi.org/10.1126/sciadv.1601755.

Wells, D. L. & Coppersmith, K. J., 1994. New empirical relationships among magnitude, rupture length, rupture width, rupture area, and surface displacement, *Bull. seism. Soc. Am.,* **84**(4), 974–1002.

Wessel, P., Smith, W. H., Scharroo, R., Luis, J. & Wobbe, F., 2013. Generic mapping tools: improved version released, *EOS, Trans. Am. geophys. Un.,* **94**(45), 409–410.

Yuan, X. *et al.*, 2000. Subduction and collision processes in the Central Andes constrained by converted seismic phases, *Nature,* **408**(6815), 958–961.

SUPPORTING INFORMATION

Supplementary data are available at *GJI* online.

Figure S1. Template matching analysis to detect earthquakes of the Calama seismic sequence. (a) Map showing the broadband stations used, the Calama earthquake with its GCMT focal mechanism, and the aftershocks reported by the CSN (red dots). (b) Frequency–magnitude diagram of the original CSN catalogue and the new catalogue with events detected through template matching (TM). (c) Normalized waveforms of the new catalogue for the vertical component of station AF01, aligned 0.5 s before the estimated *P*-wave arrival (grey dashed line). Events are sorted based on their occurrence time. (d) Daily number of events before and after the main shock.

Figure S2. Locations of the three earthquake sequences. Main shock locations are shown with stars and aftershocks with coloured circles. Upper and lower boundaries of the oceanic crust are also shown, which are less resolved at greater depths (segmented lines). (a) Absolute locations. Error bars are also shown for the main shocks. (b) Relocations obtained with a double difference method.

Figure S3. Strong motion analysis of the Calama earthquake. (a) Spatial distribution of the observed PGA at the analysed stations. The earthquake moment tensor was obtained from GCMT and is located at the epicentre. The trench line was obtained from Bird (2003). (b) Z_t residuals for PGA and SA(T) at three different periods, which are shown in different colours for each GMM. Hypocentral distance (R_{hypo}) is used by both GMMs for intraslab earthquakes. The maximum calibration distance of the GMMs is shown by the red lines.

Figure S4. Convergence of the 10 parameters of the dynamic rupture model and κ. All sampled models are shown by dots coloured according to their misfit. The grey dashed line in each plot defines the start of the range where model parameters start to converge.

Figure S5. Histograms of the 10 parameters of the dynamic rupture model and κ, calculated within the range where model parameters start to converge (as defined in Fig. S4). Cyan curves show the best-fitting Gaussian distributions of mean μ and standard deviation σ. The values of the best model (S_0) are shown with red lines.

Figure S6. 2-D distribution between parameters of the dynamic rupture model. All sampled models are shown by dots coloured according to their misfit. The white star in each plot shows the values associated to the best model.

Please note: Oxford University Press is not responsible for the content or functionality of any supporting materials supplied by the authors. Any queries (other than missing material) should be directed to the corresponding author for the paper.

Downloaded from https://academic.oup.com/gji/article/232/3/2070/6795288 by CNRS user on 11 May 2023